SECONDARY FLOW IMPACT ON VELOCITY AND THERMAL FIELDS OF A STRUCTURED TURBULENT CHANNEL FLOW

A. Stroh, K. Schäfer, P. Forooghi, B. Frohnapfel

Institute of Fluid Mechanics, Karlsruhe Institute of Technology, Karlsruhe, Germany
*E-mail: alexander.stroh@kit.edu

ABSTRACT

Surface structuring in form of streamwise elongated triangular ridges is investigated in a framework of a fully developed turbulent channel flow at $\text{Re}_b = 18000$. The ridges generate a strong large-scale secondary motion and hence alter momentum and heat transfer in the channel. A comparison of the obtained skin friction and heat transfer coefficients reveals a 30% enhancement for both quantities relatively to the smooth channel. Tripe decomposition analysis of the total stress and heat flux results in an observation of different mechanisms behind this enhancements: while the skin friction coefficient is mainly increased by the secondary-motion-related contribution, the heat flux is similarly enhanced by the secondary motion and modification of turbulent properties of the flow.

INTRODUCTION

Prandtl's secondary flows of the second kind are known to be generated in turbulent boundary layer flows with spanwise heterogeneity of the wall surface [1, 2, 3]. The motions are large-scale vortical structures (order of the boundary layer thickness) appearing in the plane normal to the primary flow direction. They extend to the outer flow layer and can significantly modify the mean velocity profile of the primary flow as well as the turbulence properties throughout the boundary layer. This type of motions has been observed in experiments and simulations of turbulent wall-bounded flows over superhydrophobic surfaces (SHS) with streamwise-elongated slip stripes [4, 5], turbulent flows over spanwise inhomogeneous rough surfaces [6] and in turbulent duct flows [7]. It is expected that the introduced modification of the flow field inherently translates into an alteration of the momentum and heat transfer throughout the channel. The present contribution considers a detailed analysis of the secondary motions above a surface with streamwise elongated triangular sharp ribs at spanwise separation of approximately one channel height. In the study we elucidate the effect of secondary motion formation on the statistical quantities of the velocity and thermal fields. Furthermore, we clarify the induced alteration of the skin friction and heat transfer coefficient by the presence of secondary motion.

Nomenclature

c_p	[J/(kg K)]	specific heat capacity
C_f	[-]	skin friction coefficient
F	[kg m / s^2]	force
h	[m]	ridge height
h_{eff}	[m]	melt-down element height
$k(z)$	[m]	surface distribution function
L	[m]	length
N	[-]	matrix dimensions
Nu	[-]	Nusselt number
Re_b	[-]	Reynolds number
Re_{Dh}	[-]	Reynolds number based on hydraulic diameter
Re_τ	[-]	friction Reynolds number
Pr	[-]	Prandtl number
P_x	[Pa/m]	mean streamwise pressure gradient
q	[W/m^2]	heat flux
St	[-]	Stanton number
ΔT_w	[K]	temperature difference
u	[m/s]	streamwise velocity
v	[m/s]	wall-normal velocity
w	[m/s]	spanwise velocity
θ	[K]	temperature (passive scalar)
u_τ	[m/s]	friction velocity
U_b	[m/s]	bulk mean velocity
W	[m]	ridge width
x	[m]	streamwise coordinate
y	[m]	wall-normal coordinate
z	[m]	spanwise coordinate
δ	[m]	half channel height
θ	[-]	dimensionless temperature
λ	[W/mK]	thermal conductivity
ν	[m^2/s]	kinematic viscosity
ρ	[kg/m^3]	density
τ	[kg/(m s^2)]	stress

Subscripts
l	lower wall
u	upper wall
min	minimum
max	maximum
ref	reference (smooth) case
tot	total
w	wall

Superscripts
+	inner (viscous) scaling

METHODOLOGY

The analysis is carried out using flow fields produced by a direct numerical simulation (DNS) in a fully developed turbulent channel flow driven at a constant flow rate (CFR). The code implementation is based on the pseudo-spectral solver with Fourier expansions in the streamwise (x) and spanwise (z) directions and Chebyshev polynomials in the wall-normal direction (y) [8]. Due to the CFR approach the bulk Reynolds number is fixed to
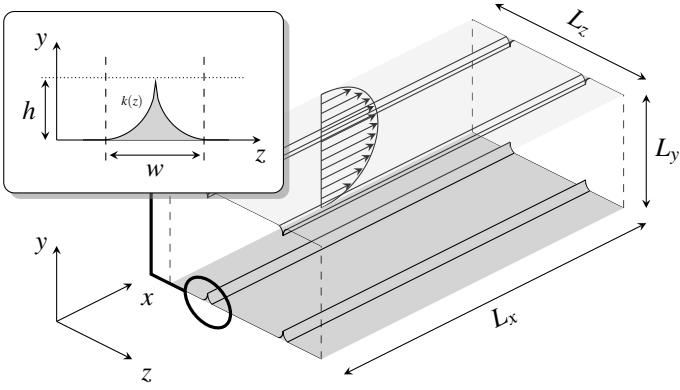
Figure 1. Simulation domain and ridge geometry.

grid size	dimensions				resolution		
$(N_x \times N_y \times N_z)$	$(L_x \times L_y \times L_z)$	Δx^+	Δy^+_{min}	Δy^+_{max}	Δz^+		
$768 \times 385 \times 384$	$8\delta \times 2\delta \times 3.72\delta$	5.2	0.016	4.0	4.7		

Table 1. Domain configuration of reference smooth case.

$Re_b = 2U_b\delta/\nu = 18000$ for all considered simulations, which means that any modification of the flow is translated into an alteration of the resulting mean streamwise pressure gradient P_x needed to maintain the chosen flow rate. Periodic boundary conditions are applied for velocity field in the streamwise and spanwise directions, while the wall-normal extension of the domain is bounded by no-slip boundary conditions at the lower and upper domain wall ($y = 0, 2\delta$). Temperature is treated as passive scalar with periodic boundary conditions applied for the thermal field in x- and z-directions, while a constant temperature on lower and upper wall is applied(T_l and T_u). This results in a fixed heat flux in the wall-normal direction. The non-dimensionalized temperature is defined as $\theta = (T_u - T)/\Delta T_w$ with $\Delta T_w = T_u - T_l$, which translates into the fixed temperature boundary condition at the lower ($\theta(y = 0) = 0$) and upper wall ($\theta(y = 2\delta) = 1$). The Prandtl number is chosen to be $Pr = 0.71$, assuming air as the working fluid. The schematic of the numerical domain is depicted in Figure 1 with corresponding simulation domain properties summarized in Table 1.

The surface geometry of an elongated triangular ridge is formed by two converging arcs with $r = 0.16\delta$ resulting in a height distribution $k(z)$ (see Figure 1). It has to be noted that the introduced structure is homogeneous in the streamwise direction. The ridges are placed on the lower and upper wall with a surface height of $h = 0.16\delta$ and spanwise width of $W = 0.32\delta$. Elevated structures are place on both channel walls and arranged symmetrically. The spanwise spacing between the ridges is given by $S = 1.86\delta$. A rather tall, sharp structure with $S \approx 2\delta$ is specifically chosen for the investigation, since this surface geometry is expected to generate a strong large-scale secondary motion in the y-z-plane of the turbulent channel flow [2]. The wall structuring is modeled by an immersed boundary method (IBM) through introduction of external volume force field to the Navier-Stokes

case	U_b^+	Re_τ	Re_b	C_f	Nu	St
smooth	18.17	495.2	18000	$6.04 \cdot 10^{-3}$	79.6	$3.11 \cdot 10^{-3}$
structured	15.66	574.5	18000	$8.09 \cdot 10^{-3}$	104.0	$4.09 \cdot 10^{-3}$

Table 2. Integral flow properties of the considered cases.

equations [9]. Throughout the manuscript the brackets $\langle \cdot \rangle$ denote spatial averaging in spanwise direction and overline $\bar{\cdot}$ represents the temporal and streamwise averaging. Additionally, the total fluctuation part is denoted with $\cdot'$, random turbulent fluctuation is marked as $\cdot''$ and dispersive fluctuation part is $\tilde{\cdot}$.
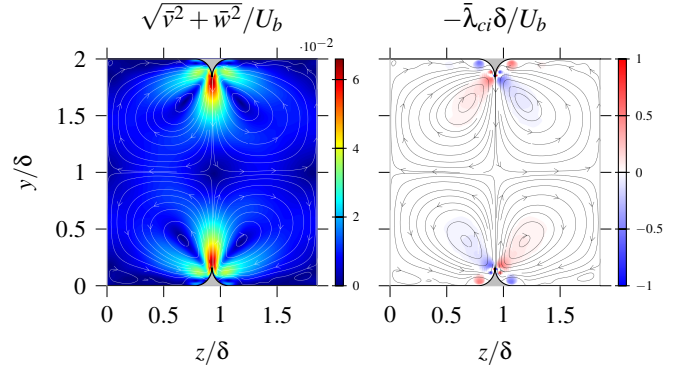
RESULTS
Secondary motion

Figure 2. Secondary flow characteristics.

The topology of the secondary flow and its magnitude is shown in Figure 2 (left). The streamwise ridges introduce a strong vortical secondary motion with a maximum local magnitude of 6.6% of the bulk mean velocity. An upward and downward motion is observed above the ridge and in the valley, correspondingly. This corresponds to the presence of counter-rotating δ-scale vortex-pair. The magnitude of the motion is rather high compared with the usual value of 2-3% known from turbulent flows over inhomogeneous rough surfaces, SHS or duct flows. This effect is linked to the geometry of the introduced wall elements - the considered elements are significantly taller ($h = 0.16\delta$) than most of the elements investigated in the literature (usually $h < 0.1$) and have a sharp top corner. Figure 2 (right) presents the mean signed swirling strength [10], which essentially shows the localization and strength of the secondary vortices in the flow domain. From this plot it is evident that the large-scale secondary motion is accompanied by small-scale tertiary vortices located at the basis of the introduced ridges. The magnitude of swirling strength in the present cases is 2-4 times higher than the values known from literature [2, 3].

Mean flow properties

Table 2 summarizes the integral properties of the considered flow configurations. Since the flow is symmetric, the mean skin friction coefficient is:

$$C_f = \tau_w/0.5\rho U_b^2 \quad \text{with} \quad \tau_w = (\delta - h_{\text{eff}})P_x, \tag{1}$$

where h_{eff} denotes the the melt down height of the surface structure and P_x is the mean streamwise pressure gradient. For the smooth and structured case $h_{\text{eff}} = 0$ and 0.0056δ, respectively. The estimated skin friction coefficient is increased by 34% for the structured surface in comparison to the smooth channel.

Statistical analysis of the thermal field also shows an enhancement of the wall-normal heat flux in the system. The Nusselt number on lower and upper wall (denoted by subscript l and u) is computed as

$$\text{Nu}_{l,u} = \frac{4\,(\delta - h_{\text{eff}})\,q_{tot}}{\Delta\theta_{l,u}\lambda} \quad \text{with} \quad \Delta\theta_l = \frac{1}{\delta}\int_0^\delta \langle\bar{u}\rangle\,\langle\bar{\theta}\rangle\,\mathrm{d}y \quad (2)$$

$$\text{and} \quad \Delta\theta_u = \frac{1}{\delta}\int_\delta^{2\delta} \langle\bar{u}\rangle\,\left(1 - \langle\bar{\theta}\rangle\right)\mathrm{d}y, \quad (3)$$

with $4\,(\delta - h_{\text{eff}})$ representing the hydraulic diameter. The total heat flux q_{tot} can be estimated as a sum of the viscous and turbulent contributions in the center of the channel:

$$q_{tot} = \lambda \left.\frac{\mathrm{d}\langle\bar{\theta}\rangle}{\mathrm{d}y}\right|_\delta - c_p\rho\,\overline{v'\theta'}\big|_\delta. \quad (4)$$

The estimated Nusselt number increases by 30% for structured surface in comparison to the smooth case. This increase in the wall-normal heat flux can be partially attributed to the presence of secondary motion. The Stanton number defined as $\text{St} = \text{Nu}/(\text{Re}_{\text{Dh}}\text{Pr})$ with Reynolds number based on U_b and the hydraulic diameter used in the definition of the Nusselt number (Equation 2) is also increased by 32% for the structured channel. The Reynolds analogy factor defined as $A = 2\text{St}/C_f$ changes slightly (order of 2%) for the smooth and structured case, respectively. This shows that Reynolds analogy factor doesn't change for the investigated structured surface with a strong secondary motion emphasizing similarity in the momentum and heat transport. This similarity is expected, since the surfaces do not introduce any additional pressure drag.

Figure 3 demonstrates mean velocity profile in inner and outer scaling (upper plot) and three components of velocity fluctuations (lower plot) for smooth (black dashed lines) and structured channel (solid colored lines). In outer scaling the mean velocity profile shows a slight suppression not only below the element hight $y < h$ in the near wall region, but also for the outer layer $y > 0.6\delta$. Due to CFR condition the reduction is balanced by a velocity increase in the region in between ($h < y < 0.6\delta$). The inner scaling, which utilizes the wall shear stress velocity u_τ of the particular case for non-dimensionalization, shows a significant reduction in $\langle\bar{u}\rangle^+$ and a clear downward shift of the logarithmic layer for the structured case. This is linked to an inherent enhancement of the effective friction Reynolds number
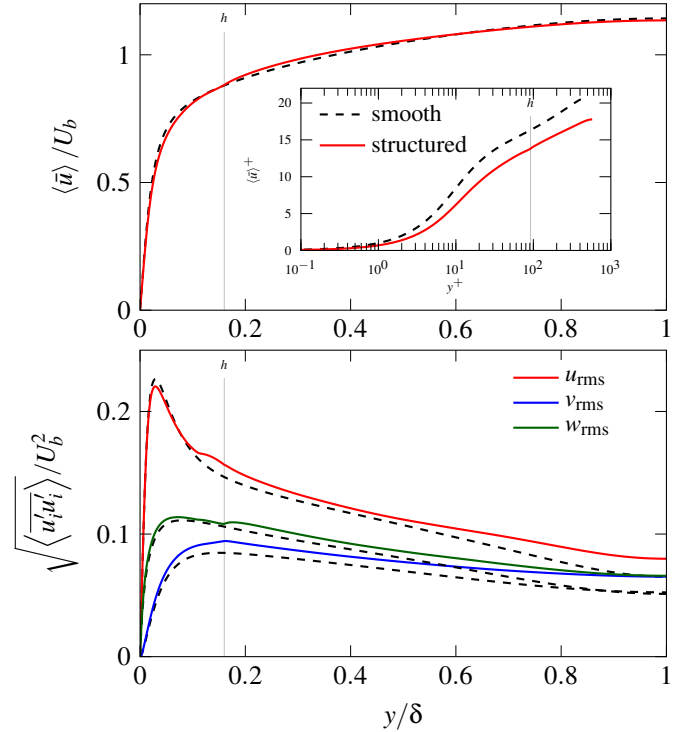

Figure 3. Velocity field statistics.

$\text{Re}_\tau = u_\tau\delta/\nu$, which originates from an increase in u_τ of the structured case. The corresponding values for non-dimensional bulk mean velocity U_b^+ und Re_τ are summarized in Table 2 for both cases. An enhancement of wall-normal and spanwise velocity fluctuations can be observed throughout the entire domain of the structured case. Streamwise velocity fluctuations show a slight reduction in the near-wall peak magnitude followed by a significant increase for $y > h$. For all three velocity components a maximal increase in the fluctuation intensities can be observed in the middle of the flow domain at $y = \delta$.

The mean temperature profile (upper plot) and temperature fluctuations (lower plot) are presented in Figure 4. A slight alteration of the mean temperature profile caused by the structuring is observed throughout the domain .A more significant modification is evident for the temperature fluctuations - while the profiles overlap up to the near-wall peaks, the rest of the curve experiences a notable increase in the bulk of the temperature field.

Triple decomposition of velocity and thermal field

In order to elucidate flow field modification linked to the secondary motion formation the triple decomposition as proposed by Reynolds & Hussain [11] is considered for the streamwise momentum balance and wall-normal heat flux. The triple decomposition of a random variable φ into mean part with dispersive ($\tilde{\cdot}$) and random ($\cdot''$) fluctuations is defined as:

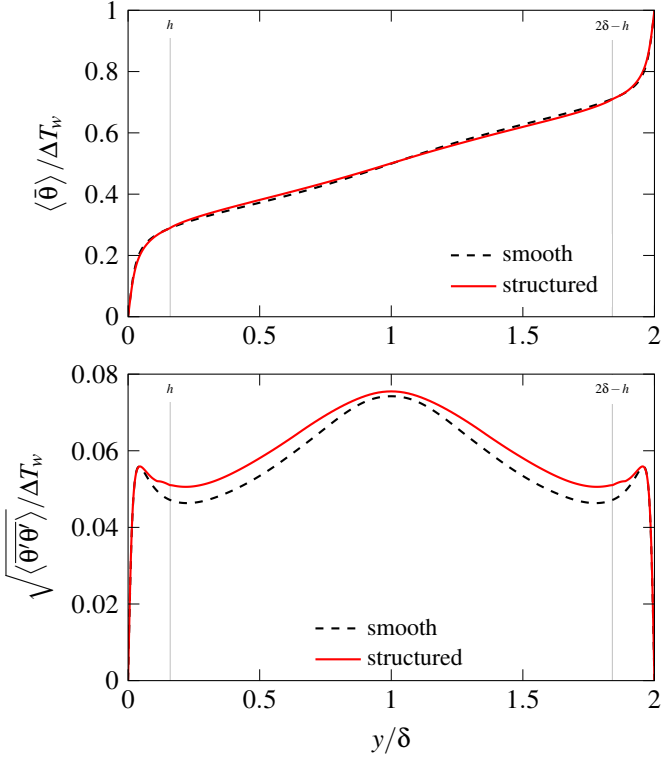$$\varphi(x,y,z,t) = \langle\bar{\varphi}_i\rangle\,(y) + \tilde{\varphi}_i(y,z) + \varphi_i''(x,y,z,t), \quad (5)$$

Figure 4. Temperature field statistics.

the streamwise momentum balance is given by:

$$\underbrace{\frac{\tau}{\tau_{w,\mathrm{ref}}}}_{\text{total}} = \underbrace{\frac{1}{\mathrm{Re}_\tau}\frac{\mathrm{d}\langle\bar{u}\rangle^+}{\mathrm{d}y^+}}_{\text{viscous}} \underbrace{-\langle\overline{u''v''}\rangle^+}_{\text{turbulent}} \underbrace{-\langle\tilde{u}\tilde{v}\rangle^+}_{\text{dispersive}} + \underbrace{\langle\bar{F}_x\rangle^+}_{\text{forcing}}, \quad (6)$$

where $\tau_{w,\mathrm{ref}}$ is the wall shear stress of the smooth channel. It has to be noted that the forcing contribution represents the volume force exerted on the fluid due the application of IBM. The temporal and streamwise averaging is denoted by $\bar{\cdot}$ and spanwise averaging is represented by $\langle\cdot\rangle$.
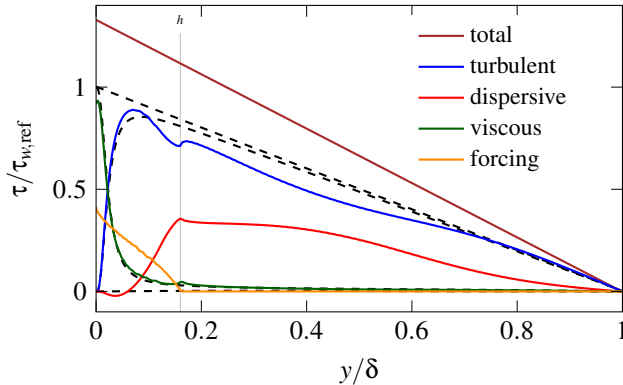

Figure 5. Triple decomposition of the total wall shear stress.

Figure 5 shows the corresponding decomposition of the total stress τ into its parts. We can observe a distinct peak for the forc-

ing term in the near-wall region and additional peaks in viscous contribution. The random turbulent part shows a very similar distribution for both smooth and structured cases. In the case of structured configuration, however, the total stress is vastly augmented by additional contribution from the dispersive fluctuations. The contribution is present throughout the wall-normal domain extension, which highlights the presence of a strong large-scale secondary flow. The contribution of the dispersive part locally exceeds 30% of the total stress ($h < y < 0.5\delta$). Interestingly, the distribution of the dispersive part shows small negative values in the near-wall region for $y < 0.1\delta$. This can be linked to the presence of small-scale tertiary vortices located at the basis of the ridge. Similar behaviour of the dispersive component is observed by Türk *et al.* [4] in a turbulent flow over superhydrophobic stripes indicating a complex topology of the secondary motion.
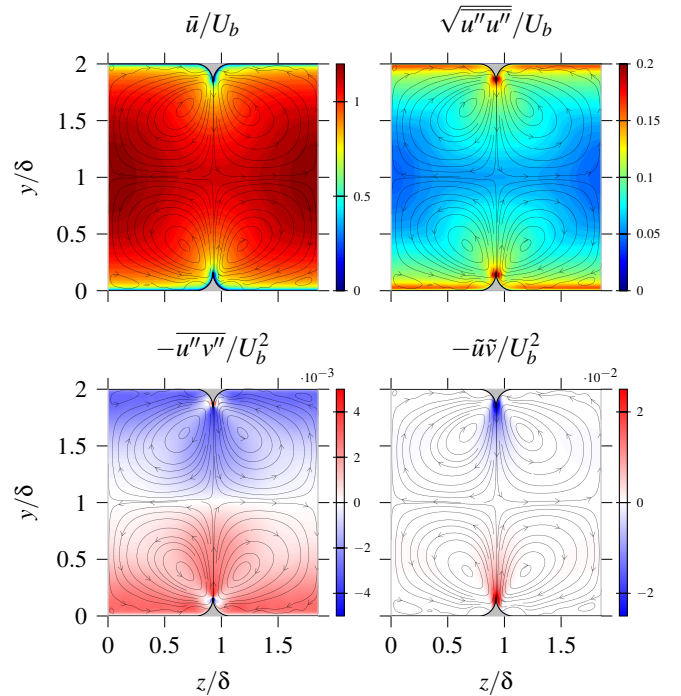

Figure 6. 2D velocity field statistics.

In order to clarify the composition of the total stress contributions we consider a two-dimensional representation of the contribution terms without spanwise averaging as shown in Figure 6 for mean velocity, streamwise fluctuations, random turbulent and dispersive components. The footprint of secondary motion is clearly visible in the mean velocity field resulting in a strong bulging above the ridge. The bulge corresponds to a low-momentum path (LMP) caused by the secondary-flow-driven upwash. Similar distribution modification is observed for $\sqrt{\overline{u''u''}}$ augmented by an additional high-intensity peak at the top of the ridge. Furthermore, one can observe a rather homogeneous distribution of $\sqrt{\overline{u''u''}}$ in the valley between ridges resembling the well know near-wall peak from a smooth channel flow configuration. The random turbulent component $\overline{u''v''}$ shows a rather

homogeneous distribution in spanwise direction. A slight augmentation of the distribution is evident above the ridge geometry and along the valley. This spanwise homogeneity coincides with the previous observation from the Figure 5, where the random turbulent contribution in the structured channel is only slightly changed relatively to the smooth channel. At the same time, the dispersive contribution $\tilde{u}\tilde{v}$ exhibits a rather strong spanwise inhomogeneity with a strong peak located above the ridge. This local peak translates into a global enhancement of the total stress for the structured case.

Application of the triple decomposition to the wall-normal balance of the heat flux yields

$$
\underbrace{\frac{q}{q_{w,\text{ref}}}}_{\text{total}} = \underbrace{\frac{1}{\text{Pr}}\frac{\mathrm{d}\langle\bar{\theta}\rangle^+}{\mathrm{d}y^+}}_{\text{viscous}} - \underbrace{\langle\overline{v''\theta''}\rangle^+}_{\text{turbulent}} - \underbrace{\langle\tilde{v}\tilde{\theta}\rangle^+}_{\text{dispersive}} + \underbrace{\langle\bar{q}_f\rangle^+}_{\text{forcing}}, \quad (7)
$$

The decomposition of the total heat flux is presented in Figure 7. Similar to the velocity field, the viscous contribution is slightly enhanced due to the introduction of the ridge geometry with the forcing contribution becoming present in the near-wall region. In contrast to the total stress, the random turbulent heat flux significantly changes for the structured channel. While the near wall region remains almost unaffected, the outer region $0.5\delta < y < 1.5\delta$ of the random turbulent heat flux experiences a pronounced augmentation. The dispersive heat flux is also prominent throughout the domain showing a fairly similar distribution to the dispersive contribution of the total wall shear stress. However, comparing the heat flux decomposition to the wall shear stress decomposition, one can state that the overall increase in the heat flux is not only governed by the dispersive contribution, but also partially originates from the enhancement of the random turbulent contribution in the outer flow. Two-dimensional counterpart of the spanwise averaged quantities, namely mean temperature, temperature fluctuations as well as random turbulent and dispersive components of the total heat flux are presented in Figure 8. The mean temperature distribution exhibits a spanwise inhomogeneity due to the structuring similar to the mean velocity. A peak of temperature fluctuations is concentrated above the ridges and can be linked to the symmetrical arrangement of the structures. Interestingly, the spanwise inhomogeneity is pronounced even stronger for the random turbulent heat flux showing a vast enhancement on the line connecting two opposite ridges. The dispersive contribution looks very similar to the dispersive contribution of the total stress a local peak above the ridge.

CONCLUSIONS & OUTLOOK

A fully developed turbulent channel flow with symmetric wall structuring is investigated with respect to alteration of skin friction and heat transfer at $Re_b = 18000$. It is shown that the introduction of streamwise aligned triangular ridges results in a strong large-scale secondary motion. At the same time we observe an enhancement of the heat transfer and skin friction coefficient by
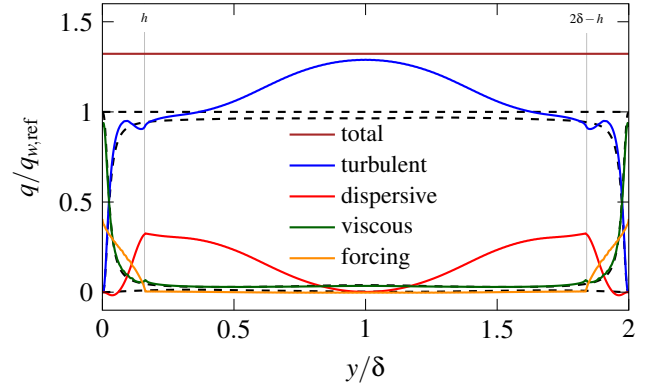

Figure 7. Triple decomposition of the total heat flux.
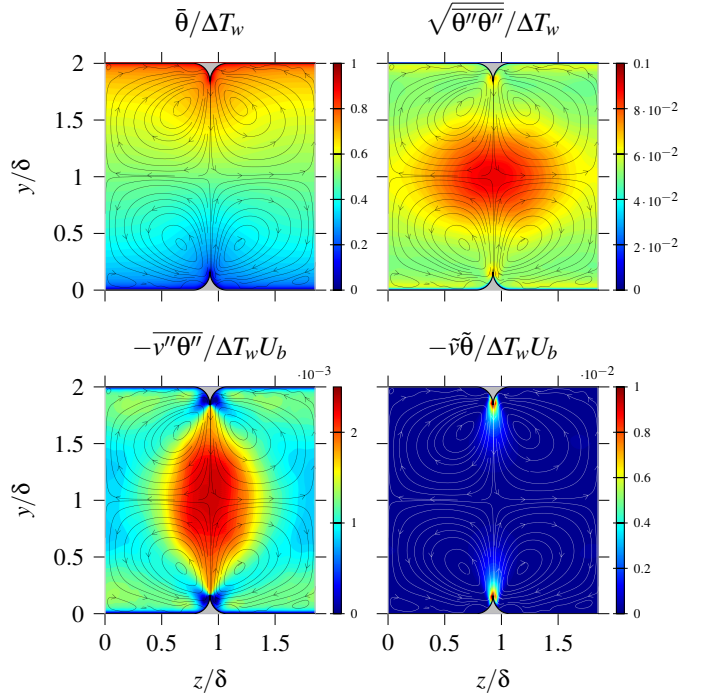

Figure 8. 2D temperature field statistics.

approximately 30%. The triple decomposition shows that the alteration of the skin friction coefficient is mainly governed by the additional dispersive component, which can be directly linked to the presence of secondary motion. As for the heat transfer coefficient, it is shown that its augmentation is linked not only to an additional dispersive contribution, but also to an enhancement of random turbulent contribution in the bulk of the flow. These differences originate from the variation of spanwise inhomogeneity introduced by the ridge geometry on the mean properties and fluctuations of velocity and thermal fields.

In the future, we plan to vary the relative position of the introduced structures in order to modify secondary motion topology and investigate the effect of the modification on the skin friction drag and heat transfer.

REFERENCES

[1] D. Willingham, W. Anderson, K. T. Christensen, and J. M. Barros. Turbulent boundary layer flow over transverse aerodynamic roughness transitions: Induced mixing and flow characterization. *Phys. Fluids*, 26(2):025111, 2014.

[2] C. Vanderwel and B. Ganapathisubramani. Effects of spanwise spacing on large-scale secondary flows in rough-wall turbulent boundary layers. *J. Fluid Mech.*, 774:1–12, 2015.

[3] C. Vanderwel, A. Stroh, J. Kriegseis, B. Frohnapfel, and B. Ganapathisubramani. The instantaneous structure of secondary flows in turbulent boundary layers. *J. Fluid Mech.*, 862:845–870, 2019.

[4] S. Türk, G. Daschiel, A. Stroh, Y. Hasegawa, and B. Frohnapfel. Turbulent flow over superhydrophobic surfaces with streamwise grooves. *J. Fluid Mech.*, 747:186–217, 5 2014. ISSN 1469-7645.

[5] A. Stroh, Y. Hasegawa, J. Kriegseis, and B. Frohnapfel. Secondary vortices over surfaces with spanwise varying drag. *J. Turbul.*, 17(12):1142–1158, 2016.

[6] H. Hwang and J. Lee. Secondary flows in turbulent boundary layers over longitudinal surface roughness. *Phys. Fluids*, 3(1):014608, 2018.

[7] M. Uhlmann, G. Kawahara, and A. Pinelli. Travelling-waves consistent with turbulence-driven secondary flow in a square duct. *Phys. Fluids*, 22(8):084102, 2010. doi: 10.1063/1.3466661.

[8] M. Chevalier, P. Schlatter, A. Lundbladh, and D. S. Henningson. Simson – A pseudo-spectral solver for incompressible boundary layer flows. Technical Report TRITA-MEK 2007-07, KTH Stockholm, Stockholm, Sweden, 2007.

[9] D. Goldstein, R. Handler, and L. Sirovich. Modeling a no-slip flow boundary with an external force field. *J. Comput. Phys.*, 105(2):354–366, 1993.

[10] C. Vanderwel and S. Tavoularis. Coherent structures in uniformly sheared turbulent flow. *J. Fluid Mech.*, 689:434–464, 2011.

[11] W. Reynolds and A. Hussain. The mechanics of an organized wave in turbulent shear flow. Part 3. Theoretical models and comparisons with experiments. *J. Fluid Mech.*, 54(2):263–288, 1972.